

Simulation of Fluid Flow and Collection Efficiency at Low Stokes Number

David L. Rigby¹

HX5, Cleveland, OH, 44135, USA

Peter M. Struk²

NASA Glenn Research Center, Cleveland, OH, 44135, USA

Numerical simulations of fluid flow and collection efficiency for a Science Engineering Associates (SEA) Robust probe are presented. The cases cover a range of freestream velocity from 10-135 m/s, and particle sizes from 1-200 μm . This combination produces results for Stokes numbers in the range of 0.07-1092. A blended modified Stokes number (defined in the paper) is introduced which covers a range of 0.07-146. Of particular interest is the collection efficiency of the sensing element (a forward-facing half-pipe), E_{tot} , in the low Stokes number regime. It was observed that the collection efficiency of the sensing area approached one for large Stokes numbers (>100) as expected. As blended modified Stokes number approached one, the E_{tot} dropped to approximately 0.5. By blended modified Stokes numbers of 0.3, the E_{tot} has dropped to essentially zero. Plotting collection efficiency versus blended modified Stokes number, the different freestream velocities collapsed quite well on to a single curve. The paper presents a discussion on the flowfield and local collection efficiency, β , in an effort to explain the predictions. Of particular interest is what is essentially a shadow zone in plain sight. As the Stokes number is reduced, the local β along the centerline of the half-pipe goes to zero. This occurs at Stokes numbers where the overall collection efficiency, E_{tot} , is still appreciable. An empirical relation was developed to allow for corrected collection efficiency values at low Stokes numbers. The correlation remains within 2% for blended modified Stokes numbers above 1, and within 6% for all cases.

I. Nomenclature

α	= Blending function = $(\tan^{-1}(A_{\text{blend}}*(St-St_{\text{shift}}))*\pi/2-1)/2$
β	= local collection efficiency
δ	= particle diameter
$\rho_{a,\infty}$	= density of air in freestream
ρ_p	= density of particle
μ	= air viscosity
A_{blend}	= coefficient in α , blending function
d_0	= obstacle scale (sensor half-pipe diameter)
E_{tot}	= Overall collection efficiency of sensing area
Re_δ	= Reynolds number based on particle diameter = $\rho_{a,\infty} U_\infty \delta / \mu$
St	= Stokes number = $\rho_p \delta^2 U_\infty / (18 d_0 \mu)$
St_M	= Modified Stokes number = $18St[Re_\delta^{-2/3} - \sqrt{6} Re_\delta^{-1} \tan^{-1}(Re_\delta^{1/3}/\sqrt{6})]$
St_M/St	= non-Stokesian drag correction factor
St_b	= Blended Modified Stokes number = $St*(1-\alpha) + St_M*\alpha$
St_{shift}	= coefficient in α , blending function
U_∞	= freestream velocity
x, y, z	= Cartesian directions

¹ Senior Research Engineer

² Aerospace Engineer, Icing Branch, 21000 Brookpark Road, AIAA Senior Member

II. Introduction

In the area of aircraft icing research, it is important to be able to characterize the cloud parameters, such as water/ice content. One technique employed involves introducing a heated element into the flow field and comparing the energy required to maintain a constant temperature to that required without a cloud. For the technique to be accurate it is important to have a good estimate of collection efficiency of the sensing area. The collection efficiency is known to depend on several characteristics of the cloud, flow, and sensor geometry. The primary dimensionless quantity used to estimate collection efficiency is the Stokes number. In addition, Bragg [1] derived a modified Stokes number, also referred to as modified inertia parameter, which is able to collapse results over a larger range of Stokes number. For large Stokes number the collection efficiency is expected to asymptote to 1.0. Lower Stokes numbers (< 1.0) can result for small particle sizes and low velocities. The small particle portion of the particle size distribution may be considered to be in the low Stokes number regime. As the flow velocity is reduced, more of the particle size distribution would reside in the low Stokes number regime.

In the present study the flow field around the Science Engineering Associates (SEA) Robust probe is simulated using the NASA in-house code GlennHT [2]. The collection efficiency is then simulated using the LEWICE3D [3,4] software. This approach was used to calculate the collection efficiency of the SEA Multi-Element Probe in 2014 [5] and the Icing Research Tunnel has included these collection efficiency corrections to their water content measurements since 2015 [6,7]. Whereas the Multi-Element Probe is designed to measure the individual signals of liquid water content and total water content, the SEA Robust probe is designed to measure total water content, whether liquid, ice, or mixed-phase. The Robust probe is made up of an aerodynamic shape that extends into the flowfield approximately 75 mm. The probe has a forward facing half-pipe which covers approximately 25 mm of the leading edge. Simulations were performed for 45 operating conditions ranging from 10-135 m/s, with particle size from 1-200 μm .

Results are presented to show local collection efficiency, as well as total sensor collection efficiency, E_{tot} . Additionally, an empirical correlation is developed which agrees with the simulations to within $\pm 6\%$ for values of E_{tot} down to 0.15, and to within $\pm 2\%$ for E_{tot} above about 0.5.

III. Description

The SEA Robust probe is a sensor that extends approximately 75 mm from the mounting surface ($z=0$). The top 1 inch (approximately 25 mm) of the span contains a forward facing half-pipe (Fig. 1).

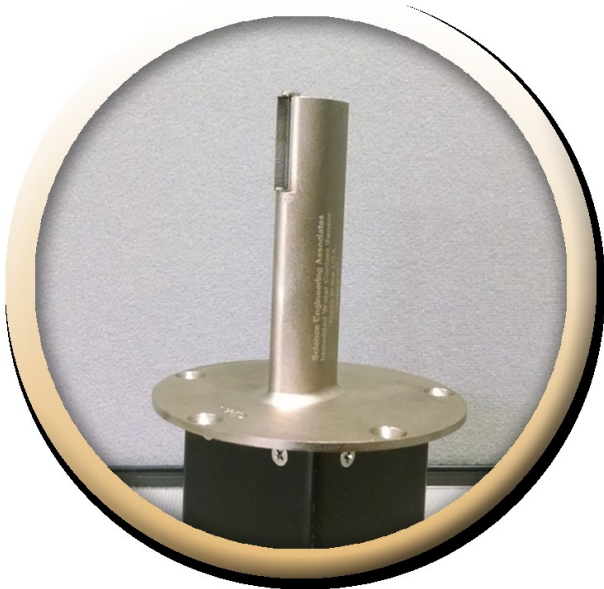


Fig. 1 Robust probe (<http://www.scieng.com/products/robust.htm>)

The flowfield around the sensor was predicted using the NASA code, GlennHT. For the sake of simplicity, and due to the limited scope of this initial study, all solid surfaces were allowed to slip. Thus, the boundary layers are not resolved. It is generally accepted that, for collection efficiency, this is a reasonable simplification. Grid resolution was chosen to be comparable to that used in previous studies on related geometries [5].

Five freestream velocities were investigated. Those values are 10, 20, 40, 85, and 135 m/s. A range of particle sizes were investigated for each velocity. The collection efficiency was calculated using the NASA code, LEWICE3D. Table 1 summarizes the cases considered, as well as some of the results which will be explained later in the paper.

Table 1 Summary of cases and overall collection efficiency

Freestream Velocity, U_∞	Particle Diameter	Stokes #	E_{tot} Sensor	non-Stokesian drag correction factor, St_M/St	Blend Function, α	Blended Modified Stokes #	E_{tot_fit}
[[m/s]]	[μm]	[-]	[-]	[-]	[-]	[-]	[-]
10	3.0	0.073	0.007	0.8723	0.1348	0.0715	-1.4999
10	4.0	0.129	0.012	0.8500	0.1484	0.1265	-0.8091
10	6.0	0.291	0.025	0.8134	0.2053	0.2800	-0.1383
10	7.0	0.396	0.050	0.7979	0.2665	0.3749	0.0446
10	8.0	0.518	0.126	0.7837	0.3767	0.4754	0.1734
10	8.5	0.584	0.210	0.7770	0.4569	0.5247	0.2222
10	9.0	0.655	0.266	0.7706	0.5480	0.5727	0.2633
10	9.5	0.730	0.310	0.7645	0.6363	0.6204	0.2993
10	10.0	0.809	0.347	0.7585	0.7103	0.6699	0.3323
10	12.0	1.164	0.446	0.7366	0.8656	0.8989	0.4466
10	13.0	1.367	0.488	0.7266	0.8991	1.0307	0.4937
10	14.0	1.585	0.526	0.7172	0.9208	1.1721	0.5349
10	16.0	2.070	0.591	0.6997	0.9467	1.4816	0.6026
10	20.0	3.235	0.685	0.6693	0.9702	2.1968	0.6980
10	25.0	5.054	0.764	0.6376	0.9824	3.2546	0.7737
10	30.0	7.278	0.818	0.6108	0.9883	4.4789	0.8235
10	35.0	9.906	0.857	0.5878	0.9916	5.8569	0.8585
10	50.0	20.216	0.921	0.5334	0.9960	10.8208	0.9192
10	100.0	80.864	0.979	0.4276	0.9990	34.6242	0.9817
10	200.0	323.457	0.991	0.3290	0.9998	106.4802	1.0017
20	5.0	0.404	0.071	0.7585	0.2723	0.3777	0.0489
20	5.7	0.525	0.171	0.7429	0.3856	0.4734	0.1712
20	6.0	0.582	0.209	0.7366	0.4543	0.5125	0.2109
20	9.0	1.310	0.463	0.6838	0.8915	0.9408	0.4627
20	13.0	2.733	0.639	0.6319	0.9632	1.7641	0.6475
40	3.5	0.396	0.079	0.7172	0.2665	0.3664	0.0312
40	4.0	0.518	0.165	0.6997	0.3767	0.4590	0.1554
40	4.2	0.571	0.198	0.6932	0.4397	0.4936	0.1923
40	7.0	1.585	0.494	0.6210	0.9208	1.0319	0.4941
40	10.0	3.235	0.660	0.5676	0.9702	1.8775	0.6625
85	2.0	0.275	0.032	0.6916	0.1979	0.2582	-0.1944
85	3.0	0.619	0.207	0.6347	0.5012	0.5054	0.2040
85	4.0	1.100	0.365	0.5922	0.8500	0.7185	0.3612
85	5.0	1.718	0.494	0.5583	0.9301	1.0124	0.4878
85	7.0	3.368	0.652	0.5066	0.9716	1.7535	0.6460
135	1.0	0.109	0.011	0.7218	0.1432	0.1048	-1.0142
135	2.0	0.437	0.087	0.6264	0.2978	0.3881	0.0644
135	2.5	0.682	0.213	0.5933	0.5818	0.5208	0.2186
135	3.0	0.983	0.297	0.5657	0.8113	0.6363	0.3103
135	4.0	1.747	0.481	0.5216	0.9318	0.9680	0.4725
135	6.0	3.930	0.671	0.4594	0.9764	1.8555	0.6597
135	8.0	6.987	0.769	0.4162	0.9877	2.9577	0.7569
135	10.0	10.917	0.830	0.3836	0.9924	4.2388	0.8156
135	20.0	43.667	0.940	0.2903	0.9982	12.7324	0.9315
135	100.0	1091.667	1.003	0.1340	0.9999	146.3809	1.0028

IV. Results

A. Flowfield

In this paper, the coordinate system used has freestream flow in the x -direction, and z going along the span of the probe. Figure 2 shows an example of the pressure field on the probe surface and on a constant z -plane. The constant z -plane is near the bottom of the half-pipe sensor at $z=54$ mm. In Fig. 2, it can be seen that the surface of the sensor is quite uniformly red, indicating that essentially all of the pressure has recovered, and the velocity is very low.

Figure 3 shows representative velocity vectors on a constant z -plane near the middle of the sensor ($z=64$ mm). In this figure it can be seen that the flow within the half-pipe region is very slow. Also, the central region of the half-pipe has flow entering, while the side regions are where the flow escapes.

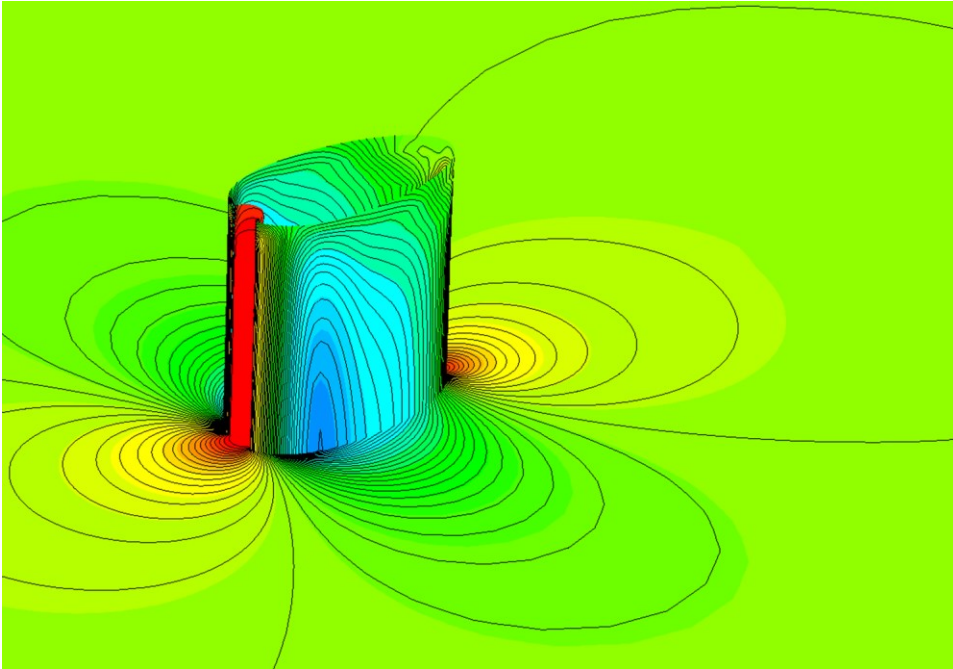


Fig. 2 Probe surface and constant z -plane (near bottom of sensor, $z=54$ mm) colored by pressure.

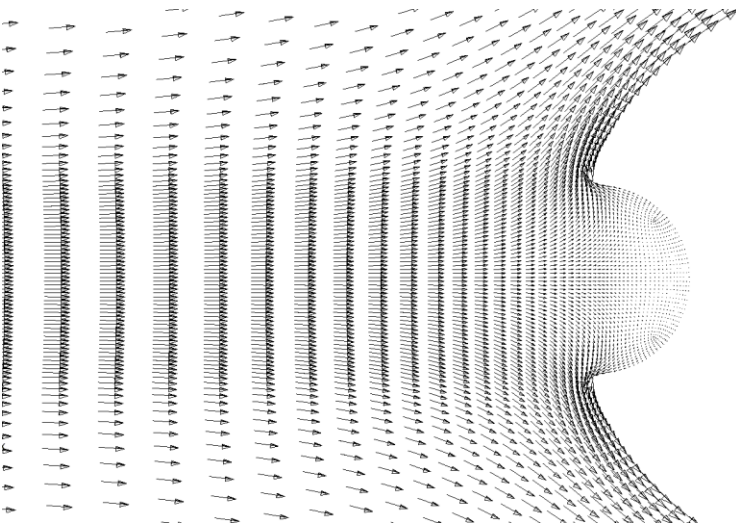


Fig. 3 Velocity vectors on constant z -plane near middle of sensor ($z=64$ mm).

B. Local Collection Efficiency, beta

Figures 4-9 show the surface of the probe colored by local collection efficiency, beta. These figures represent a sampling of the results and show the characteristics of the changes that occur as Stokes number is reduced. Figures 4-6 are at freestream velocity of 135 m/s, while Figures 7-9 are at 10 m/s.

Figure 4 shows the case at high velocity (135 m/s) and large particle diameter (100 μm). In this case, the particles are not able to deviate much from their freestream path and the collection efficiency is high. Note, the black lines represent five span locations where line plots will be presented in a later section.

In Fig. 5, the particle size has been reduced by a factor of 10 relative to Fig. 4. Now the particles are better able to avoid the obstacle and the collection efficiency is reduced.

In Fig. 6, the particle size is now very small, 3 μm . It can be seen that the collection efficiency on the leading edge below the sensor is less than 0.35. Of particular interest is that a region, at the bottom of the half-pipe, has essentially been reduced to zero collection efficiency. However, on the sides of the half-pipe the collection efficiency is still significant. Later figures will quantify this observation.

Figure 7 shows the local collection efficiency for the case of 10 m/s and 100 μm . In this case the collection efficiency is quite high, but as will be shown, more quantitatively later, is lower than the 135 m/s case as expected.

Figure 8 shows the case of 10 m/s and 10 μm . Here the collection efficiency is significantly reduced compared to Fig. 7, and the region of zero collection efficiency has appeared at the bottom of the half-pipe (as it did in Fig. 6 at higher velocity and smaller particle size). Figure 9 shows the same result as Fig. 8 but zoomed in and showing grid lines. From Fig. 9 it is apparent that there is a distinct region at the bottom of the half-pipe where the collection efficiency is essentially zero. Another intriguing observation is that, on the sides of the half-pipe there is appreciable collection efficiency. There is appreciable collection efficiency over a region below the sharp edge where the half-pipe meets the rest of the probe. In addition, there is a spike in the collection efficiency between the relatively constant region and the essentially zero collection efficiency region.

Figures 10 and 11 present line plots of collection efficiency, beta, versus y. Each plot contains five lines, each one corresponding to the black lines seen in the previous three dimensional views. The values $z=34$ mm and $z=44$ mm are the two lines below the sensor. The values $z=54$ mm, 64 mm, and 74 mm cut through the sensing area, near the bottom, middle, and tip, respectively. Recall that $z=0$ is the mounting surface.

Figure 10 shows the results for, freestream velocity of 135 m/s, at six different particle sizes. It is interesting to compare the lines below the sensor to the lines that cut through the sensor area. The lines below the sensor are relatively flat in the center, owing to the flat leading edge. The lines that cut through the sensing area tend to look like half of a cosine curve (especially at the larger particle sizes) in the center. This is to be expected simply because of the angle that the sides of the half-pipe make to the freestream direction. As the particle size is reduced, the behavior of the curves begin to deviate significantly from the expected large particle behavior. As the particle size is reduced, the collection efficiency at the center of the half-pipe is reduced, while the side regions (absolute value of y in the range 1 to 1.5) actually increase. At the smallest particle size 3 μm the collection efficiency is essentially zero near the center of the half-pipe. It is very interesting to note, as shown in table 1, the overall collection efficiency for this case is still $E_{\text{tot}}=0.297$.

Figure 11 shows some results for the 10 m/s cases. At the large particle size the shape of the curves are as expected. Behavior similar to the results at 100 m/s are observed, except that it appears at larger particle sizes for the 10 m/s cases. For the 10 μm case a plot is included with a scale that matches all the other plots in Figures 10 and 11. In addition, a plot is included with scale on beta expanded to include the full range of values. This expanded scale plot demonstrates the concentration of particles to the sides of the half-pipe.

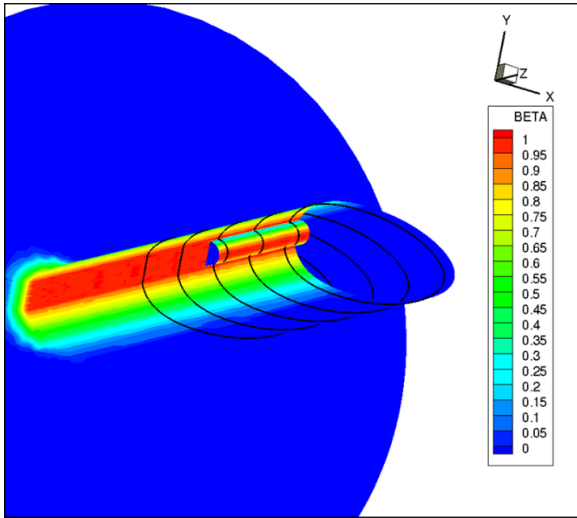


Fig. 4 Surface colored by beta: $U_\infty=135$ m/s, $d=100$ μ m.

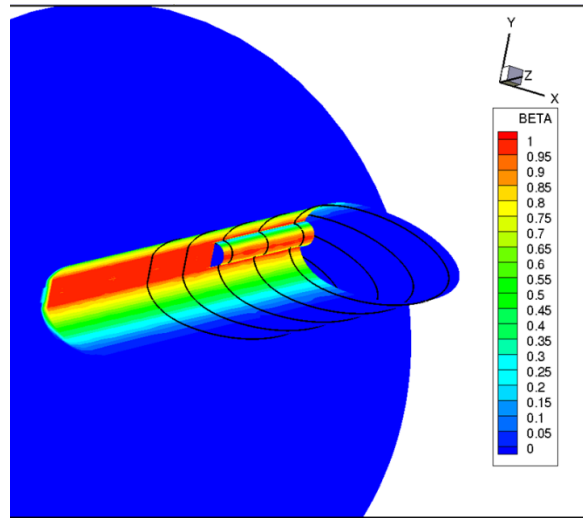


Fig. 7 Surface colored by beta: $U_\infty=10$ m/s, $d=100$ μ m.

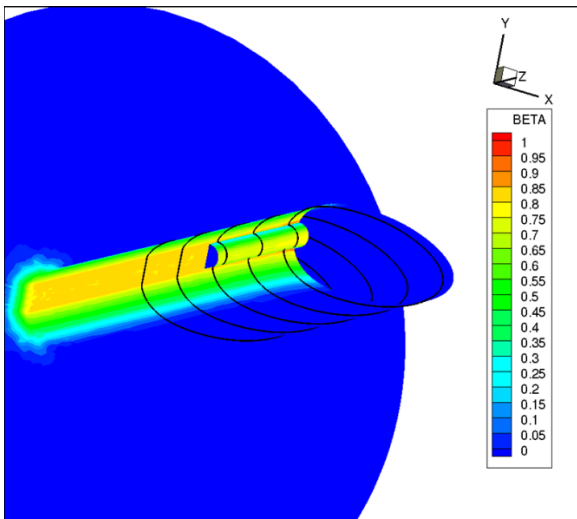


Fig. 5 Surface colored by beta: $U_\infty=135$ m/s, $d=10$ μ m.

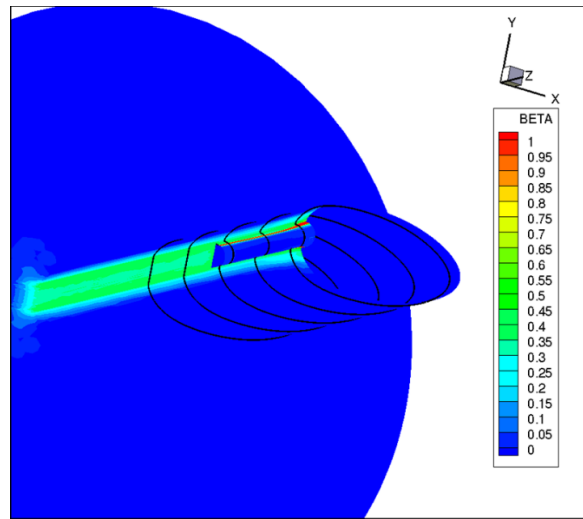


Fig. 8 Surface colored by beta: $U_\infty=10$ m/s, $d=10$ μ m.

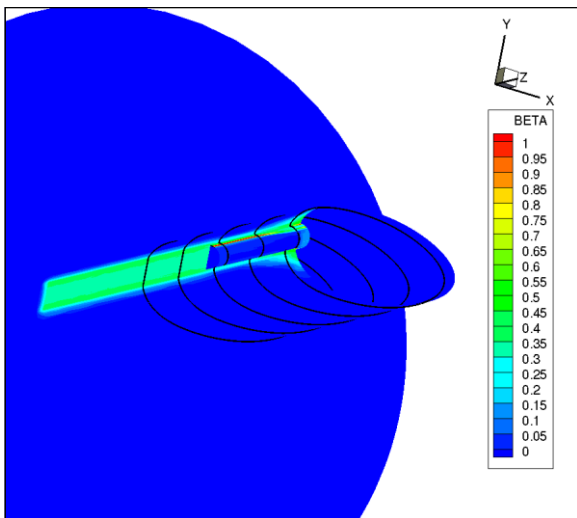


Fig. 6 Surface colored by beta: $U_\infty=135$ m/s, $d=3$ μ m.

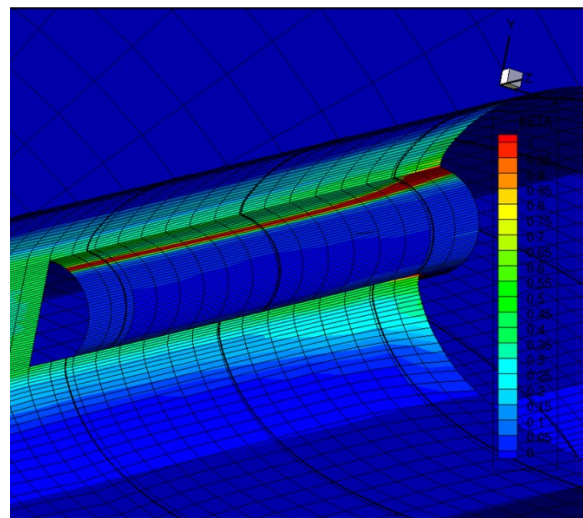


Fig. 9 Zoomed in: $U_\infty=10$ m/s, $d=10$ μ m.

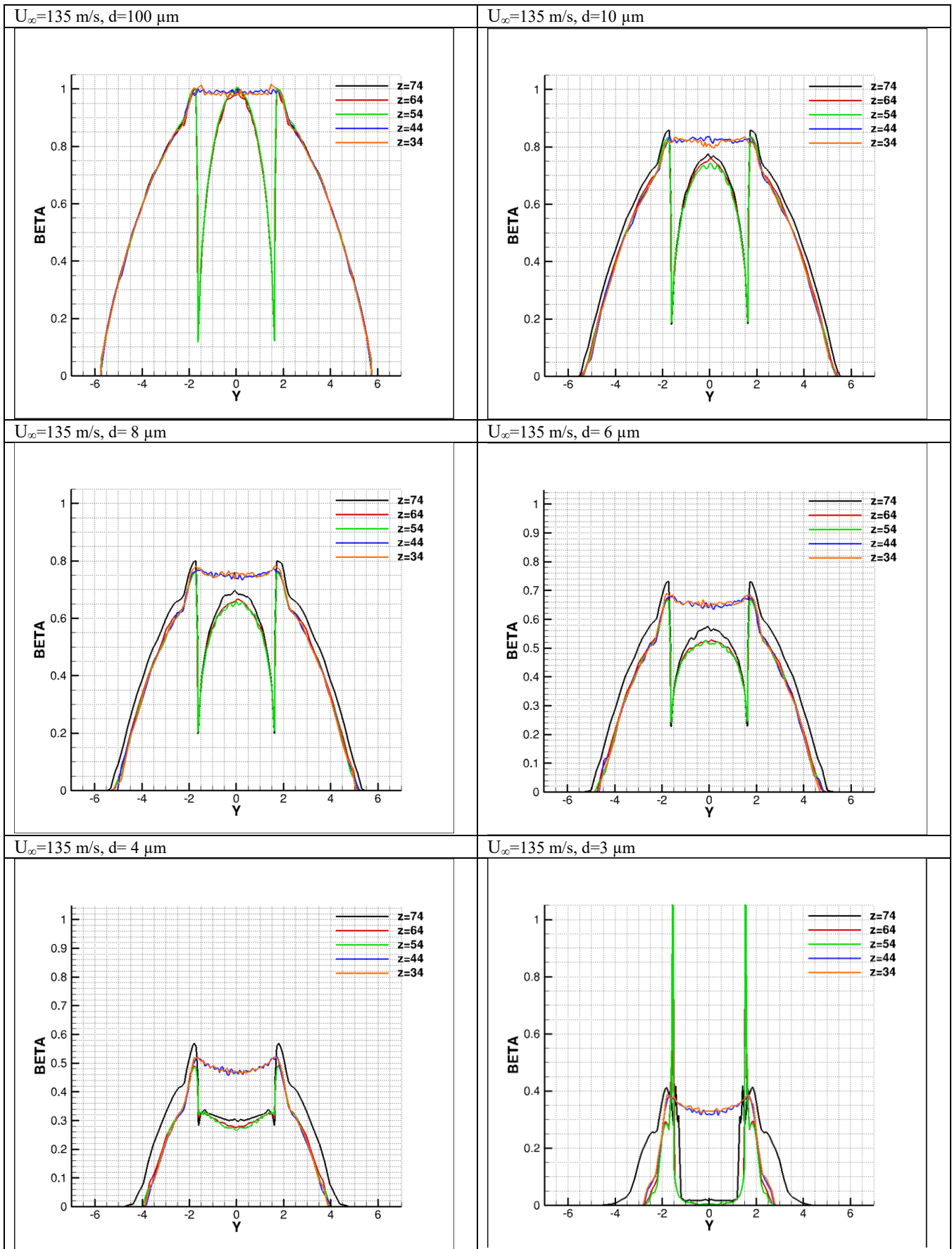


Fig. 10 beta vs Y, $U_\infty = 135$ m/s

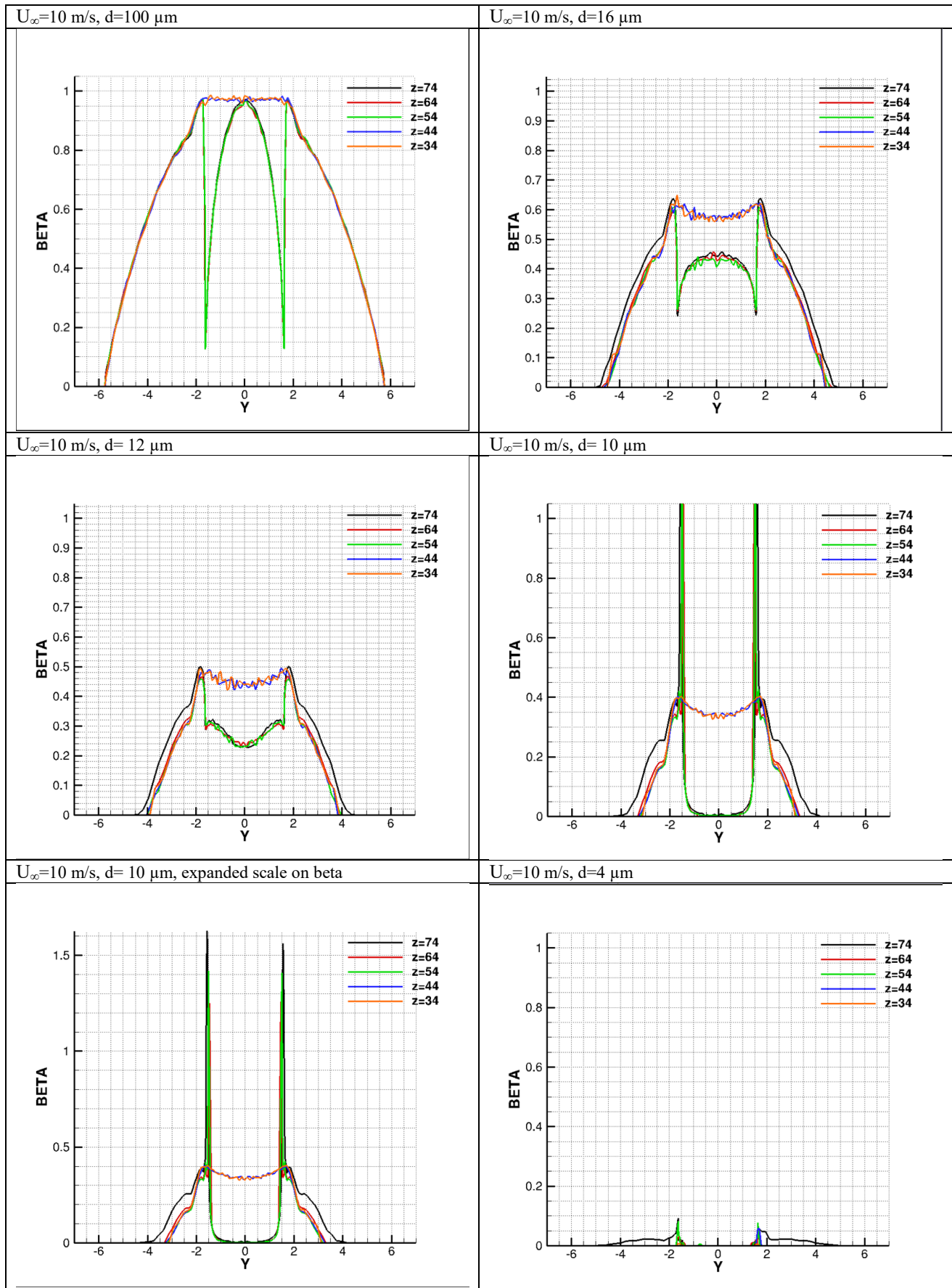


Fig. 11 beta vs Y, $U_\infty = 10$ m/s

C. Overall Collection Efficiency, E_{tot}

While it is interesting to look at local collection efficiency, in the end the total collection efficiency, E_{tot} , over the sensing area is of most interest. In this section, results for the total collection efficiency will be presented and discussed. In addition, an empirical equation is developed that should prove useful for experimental post-processing.

It is quite common to plot E_{tot} against a modified Stokes number, St_M in an effort to make the data collapse for various particle sizes, densities and velocities. The modified Stokes number (also known as the modified inertia parameter) follows that derived by Bragg [1]

$$St_M = 18St \left[Re_\delta^{-2/3} - \sqrt{6}Re_\delta^{-1} \tan^{-1} \left(\frac{Re_\delta^{1/3}}{\sqrt{6}} \right) \right] \quad (1)$$

$$Re_\delta = \frac{\rho_{a,\infty} U_\infty \delta}{\mu_{a,\infty}} \quad (2)$$

$$St = \frac{\rho_p \delta^2 U_\infty}{18d_o \mu_{a,\infty}} \quad (3)$$

When the results from the present simulation were plotted against modified Stokes number two things were observed. First, data at higher Stokes number *did* collapse better, as compared to using the standard Stokes number. Second, the data at the lowest modified Stokes numbers did not collapse well.

At first, it was considered that some additional modification to the Stokes number was warranted. In the end, that is essentially what was done. However, it was not an additional modification, but rather a subtraction of the effect of the modified Stokes number at low Stokes number. It was realized that the results collapse better at the lowest Stokes numbers when the Stokes number is not modified. In hindsight this makes sense because the modification is known to help at higher Stokes numbers. The modified Stokes number does approach the standard Stokes number as Stokes number becomes small, but this does not occur until values are much smaller than 1.

To provide for an explicit blending between the modified and standard Stokes numbers, a new blending function was introduced. The blended modified Stokes number is defined as:

$$St_b = St*(1-\alpha) + St_M*\alpha \quad (4)$$

$$\alpha = (\tan^{-1}(A_{blend}*(St - St_{shift})) * \pi/2 - 1)/2 \quad (5)$$

The constants A_{blend} and St_{shift} are chosen to optimize the collapse of data over the entire Stokes number range. The appropriate values for the constants were determined as part of the empirical curve fitting process.

To best fit the results from the simulation, a function with the following form was chosen:

$$E_{tot,fit} = A_{fit} + B_{fit}*(St_b)^p + C_{fit}*(St_b)^q \quad (6)$$

The coefficients, A_{fit} , B_{fit} , C_{fit} , as well as the powers p and q , are determined by a least square optimization. Note that as part of the optimization, A_{blend} and St_{shift} are also determined. To perform the least square fit; the Microsoft Excel Solver functionality was employed. All of the cases summarized in table 1 were included, except cases which produced E_{tot} below 0.15. It is expected that E_{tot} should asymptote to 1 as Stokes number gets large. Because of this expectation, for E_{tot} to asymptote to 1, an additional constraint was placed on the curve fit. The additional constraint requires that the curve fit pass through 1.0 at St_b of 300. The expectation here is that beyond values of 300 a value of $E_{tot} = 1$ is expected and the curve fit can be abandoned.

The final result from the least square fit is:

$$E_{tot,fit} = 1.909 - 0.6903*(St_b)^{-0.5208} - 0.7353*(St_b)^{0.0302} \quad (7)$$

$$\alpha = (\tan^{-1}(4.054*(St - 0.6180)) * \pi/2 - 1)/2 \quad (8)$$

Figure 12 shows a plot of overall collection efficiency, E_{tot} , for the cases shown in table 1, plotted against the blended modified Stokes number. It is interesting to note that plotting against blended modified Stokes number very effectively collapses the five freestream velocities considered. At a blended modified Stokes number of one the collection efficiency has been reduced to approximately 0.5. Below modified Stokes number of 0.1 the collection efficiency is essentially zero. The empirical curve fit is within $\pm 6\%$ for all values of E_{tot} above 0.15, and within $\pm 2\%$ for values of E_{tot} above 0.5.

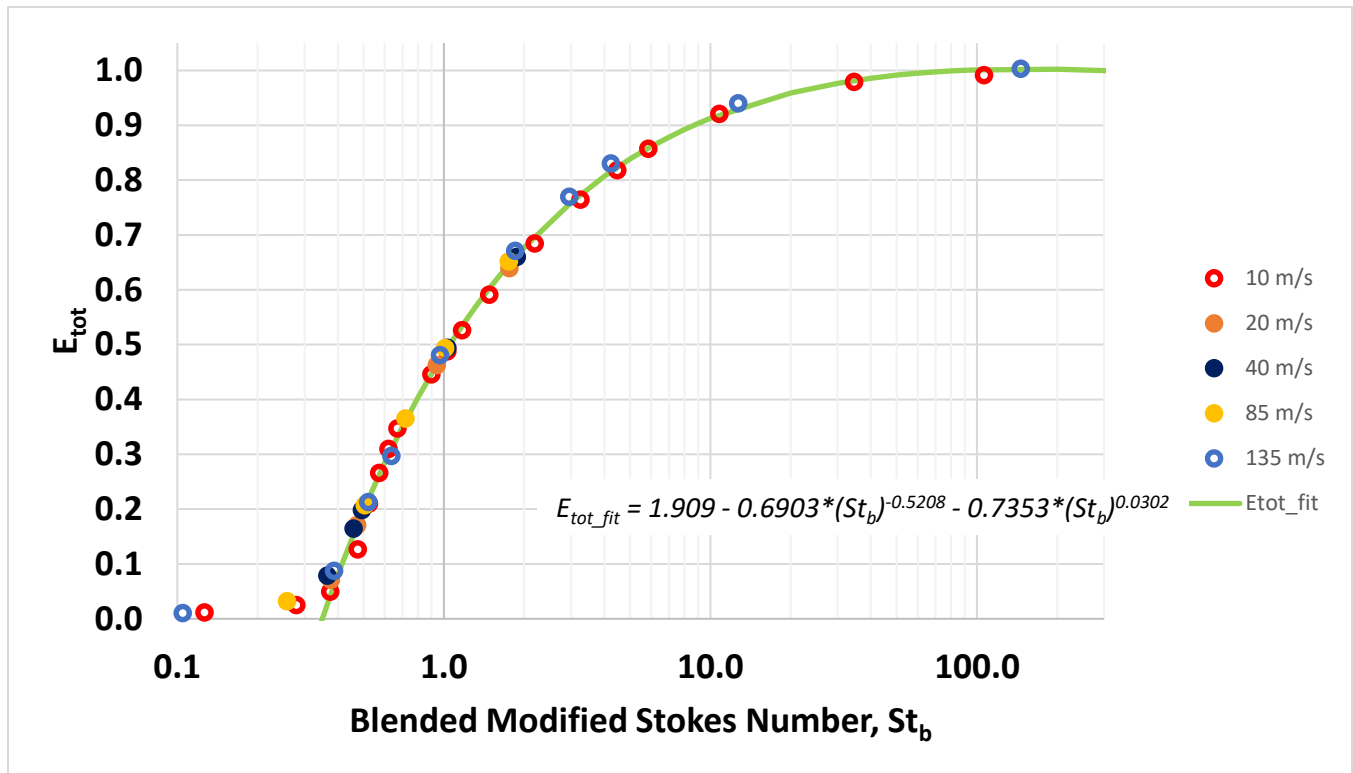


Fig. 12 E_{tot} vs Blended Modified Stokes Number

Figure 13 shows an assessment of how well the empirical curve fits all the results. To demonstrate why two power terms are included, and why the blended Stokes number is introduced, results from other choices are included. Figure 13a shows the error that results if the standard Stokes number and a single power term is used for the least square fit. The error in Fig. 13a is large across the range of Stokes number. It does not drop below 5% and becomes significantly worse for low Stokes numbers. In fact, two data points for the 135 m/s results are not shown because they are below the lower limit in the graph. Figure 13b shows the improvement by using modified Stokes number. The results are markedly improved, but the desire to fit low and high values of Stokes number results in around 5% error over much of the range. In addition, the single power, modified Stokes number does a poor job at the very lowest Stokes numbers. The addition of the second power term allows for significant improvement above Stokes numbers of 1, but still produces deviations of nearly 15% for the lowest values. Finally, Fig. 13d shows the results which include two power terms, as well as the blending function from standard Stokes at low Stokes number to modified Stokes at higher Stokes numbers. The errors shown in Fig. 13d correspond to the curve fit in Fig. 12. The errors in Fig. 13d are maintained below $\pm 6\%$ for all cases with E_{tot} greater than 0.15. For blended modified Stokes numbers above 1 the error remains below $\pm 2\%$.

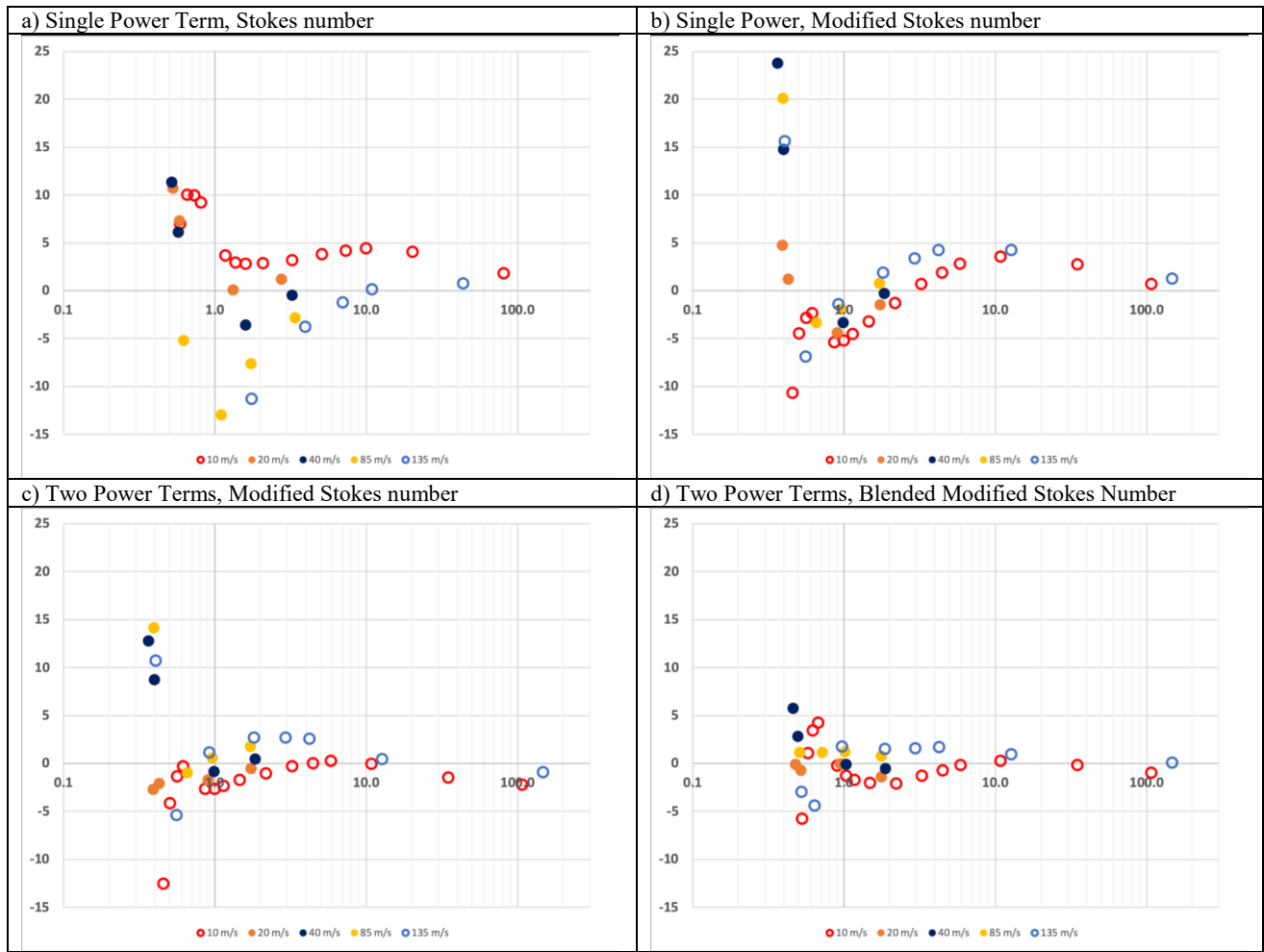


Fig. 13 Percentage fit error vs particle size for various methods

V. Conclusion

A numerical investigation of the collection efficiency characteristics of the SEA Robust probe was carried out. A particular focus of the study was when the collection efficiency becomes significantly less than one. Low values of collection efficiency can occur at small particle size and at low velocities. The present study included particle sizes ranging from 1-200 μm , and freestream velocities in the range 10-135 m/s. This combination produces results for Stokes numbers in the range of 0.07-1092. A blended modified Stokes (defined in the paper) is introduced which covers a range of 0.07-146.

The main objective of the study was to investigate the total collection efficiency in the sensor region as Stokes number is reduced. As part of the investigation, the local collection efficiency was examined. A particularly interesting phenomena was observed as the Stokes number was reduced. The pocket of air just upstream of the half-pipe is seen to be essentially a dead zone of low velocity air. At low Stokes numbers the particles are unable to penetrate to the center of the half-pipe before being diverted to one side or the other. The net result is a shadow zone in plain sight. That is to say, the area of the half-pipe is easily visible from upstream and yet the local collection efficiency goes to zero. The particles that are diverted to either side end up impinging on the sides of the half-pipe which creates large collection efficiencies in those areas.

A total of 45 cases were simulated and their total collection efficiency, E_{tot} , extracted for the sensor area. In an effort to develop a reasonable empirical correlation; any case with E_{tot} above 0.15 was included in a least square optimization. A total of 35 cases were used in the least square optimization. A correlation was developed which remains within $\pm 6\%$ for all cases with E_{tot} greater than 0.15, and within $\pm 2\%$ for cases with E_{tot} above about 0.5. To achieve good collapse of the results required two key elements. First, the equation chosen includes a constant plus two additional terms in which both the coefficient as well as the power that the Stokes number is raised to are optimized. Second, a blended modified Stokes number was introduced. It was observed that the traditional modified Stokes number did not progress back to the standard Stokes number quickly enough as Stokes number became small. So, a blending function was introduced which remains closer to the standard Stokes number for larger values of Stokes number, then migrates toward the modified Stokes number.

Acknowledgments

This work is supported by the Advanced Aircraft Icing (AAI) Subproject of the NASA Advanced Air Transport Technology Project (AATT) under NASA's Advanced Air Vehicle Program (AAVP). The authors would also like to thank Anthony Nerone, manager of the NASA Advanced Aircraft Icing subproject for supporting this work.

References

- [1] Bragg, M. B. "A similarity analysis of the droplet trajectory equation," AIAA Journal Vol. 20, No. 12, 1982. pp. 1681-1686.
- [2] Steinthorsson, E.; Liou, M.S.; and Povinelli, L.A.: Development of an Explicit Multiblock/Multigrid Flow Solver for Viscous Flows in Complex Geometries. AIAA-93-2380 (NASA TM-106356), 1993.
- [3] Wright, W. B., "Users Manual for the NASA Glenn Ice Accretion Code LEWICE Version 3.0," available on the NASA LEWICE 3.0 release CD, April 2003.
- [4] Bidwell, C.S., and Potapczuk, M.G., "Users Manual for the NASA Lewis Three-Dimensional Ice Accretion Code (LEWICE3D)," NASA TM 105974, 1993.
- [5] Rigby, D. L., Struk, P. M., and Bidwell, C. S. "Simulation of fluid flow and collection efficiency for an SEA multi-element probe," 6th AIAA Atmospheric and Space Environments Conference, AIAA-2014-2752, Atlanta, GA, 2014. doi: 10.2514/6.2014-2752
- [6] Steen, L.E., Ide, R.F., Van Zante, J.F., and Acosta, W.J., "NASA Glenn Icing Research Tunnel: 2014 and 2015 Cloud Calibration Procedures and Results" NASA TM 218758, 2015.
- [7] Steen, L. E., Ide, R. F., and Van Zante, J. F. "An Assessment of the Icing Blade and the SEA Multi-Element Sensor for Liquid Water Content Calibration of the NASA GRC Icing Research Tunnel," 8th AIAA Atmospheric and Space Environments Conference, AIAA-2016-4051, Washington, DC, 2016. doi: doi:10.2514/6.2016-4051